Diversity selection for phase-diverse phase retrieval

Bruce H. Dean

Optics Branch: Design & Analysis Group/Code 551, NASA/Goddard Space Flight Center, Greenbelt, Maryland 20771

Charles W. Bowers

UV/Optical Astronomy Branch/Code 681, NASA/Goddard Space Flight Center, Greenbelt, Maryland 20771

Wavefront-sensing performance is assessed for focus-diverse phase retrieval as the aberration spatial frequency and the diversity defocus are varied. The analysis includes analytical predictions for optimal diversity values corresponding to the recovery of a dominant spatial-frequency component in the pupil. The calculation is shown to be consistent with the Cramér–Rao lower bound by considering a sensitivity analysis of the point-spread function to the spatial frequency being estimated. A maximum value of diversity defocus is also calculated, beyond which wavefront-sensing performance decreases as diversity defocus is increased. The results are shown to be consistent with the Talbot imaging phenomena, explaining multiple periodic regions of maximum and minimum contrast as a function of aberration spatial frequency and defocus. Wavefront-sensing performance for an iterative-transform phase-retrieval algorithm is also considered as diversity defocus and aberration spatial frequency are varied.

OCIS codes: 100.5070, 120.5050, 110.6760.

1. INTRODUCTION

Phase-diverse phase retrieval is an image-based wavefront-sensing method that utilizes point-source images modulated in a controlled way (i.e., with a diversity function[1]) to recover optical phase information. In principle, any known aberration can serve as a diversity function, but defocus is often the simplest to implement and exhibits no angular dependence as a function of the pupil coordinates.[2] In earlier analysis,[3–5] certain defocus settings have been shown to enhance phase-retrieval estimation performance based on numerical calculations of the Cramér–Rao lower bound (for general references on the Cramér–Rao bound, see Refs. 6–9; additional applications to wavefront sensing are addressed in Refs. 10–12). But no general predictions have been derived to show which diversity values are optimal for a given wavefront-sensing application or even to motivate a general understanding of why certain defocus values are preferable to others. In this paper, a theoretical basis for the phenomena is discussed, as well as how optimal diversity functions can be utilized to enhance phase-retrieval estimation performance. An important corollary result is that proper diversity selection really defines how wavefront sensing and control should be implemented, i.e., systems that are designed for lower-spatial-frequency recovery should be distinguished from those designed to recover higher-spatial-frequency aberrations.[13,14] This viewpoint provides a general guide for understanding how diversity functions should be implemented and is discussed further in Section 10.

To motivate the approach discussed in the paper from the perspective of wavefront-sensing algorithms, Fig. 1 depicts the mechanism of classical iterative-transform phase retrieval (termed "error reduction" in the earlier literature[15]), which operates by iteratively enforcing constraints between conjugate Fourier domains. A phase map is thus produced that is consistent with the measured data in both domains to within some convergence criterion. This basic mechanism gives a simple picture of how good contrast in the aberration "signals" can lead to improved wavefront-sensing performance. Conversely, if the data have low signal-to-noise ratio or if the aberration content is only weakly coupled to the intensity data (or both), convergence can be slow or yield inaccurate results. This conceptual framework applies to other estimation methods as well; e.g., parametric phase retrieval (e.g., Ref. 16) attempts to minimize an objective function O with respect to the unknown aberration parameters. If the objective function is weakly coupled to the data, then, similarly, the gradient of the objective function will exhibit a weak functional dependence with respect to the parameters being estimated. In such cases, a numerical solution minimizing O may converge slowly or yield inaccurate results. A quantitative numerical description of the viewpoint described above follows from the Cramér–Rao lower bound, which is discussed further in Section 7.

The paper is organized as follows: In Section 2, the spectral power corresponding to a defocused phase grating is calculated. In Section 3, these results are applied to derive optimal diversity defocus values that yield maximum contrast in the spectral power for image-based wavefront sensing. A maximum value of diversity defocus is also calculated in Section 4, beyond which wavefront-sensing performance decreases as diversity defocus is increased. In Section 5, the fundamental role played by diffraction in the recovery of aberration infor-
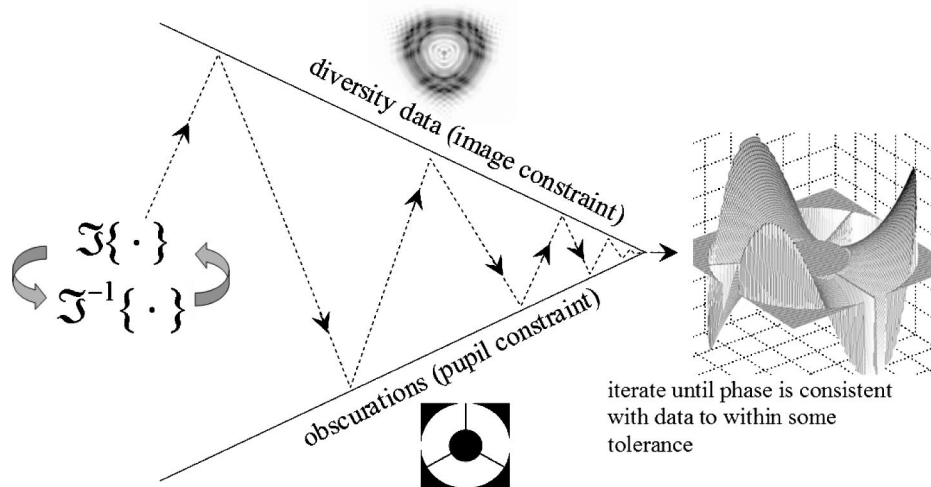
Fig. 1.   Iterative-transform phase retrieval [$\mathcal{F}(\cdot)$ denotes Fourier transform].
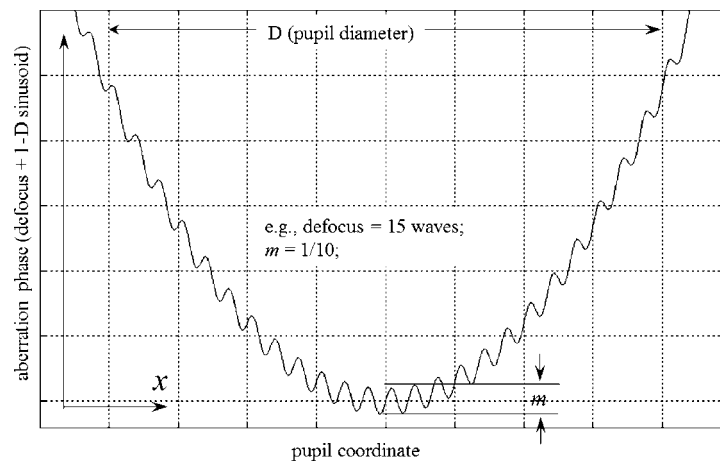

Fig. 2.   Defocus + sinusoidal "aberration."

mation is emphasized, and the alternating contrast maxima and minima that occur in the spectral power as a function of defocus are shown to be consistent with the Talbot imaging phenomena. In Section 6, a transfer function analysis is presented to locate "windows" of peak response as a function of spatial frequency and defocus. In Section 7, consistency with the Cramér–Rao lower bound is discussed. Wavefront-sensing performance is discussed in Section 8 to demonstrate that proper diversity selection can lead to improved wavefront-sensing convergence and accuracy when utilizing iterative-transform phase retrieval. Finally, in Section 9, a dominant spatial frequency for the Zernike basis functions of a given order is calculated. These results are then applied to derive optimal diversity defocus values as a function of Zernike order.

## 2. SPECTRAL POWER OF A DEFOCUSED PHASE GRATING

Consider the calculation of image irradiance in a defocused image plane when the exit pupil of the system is conjugate to a phase grating (phase gratings are discussed, for instance, in Ref. 17; earlier analysis on the

propagation of spectral power utilizing a phase grating in the context of wavefront sensing has been presented in Refs. 18–20). This model is particularly relevant when considering the wavefront spatial-frequency content of systems with deformable mirrors,[21] in addition to being convenient for analytical work.

Assuming a monochromatic point source, the calculation is modeled as a Fresnel propagation through an arbitrary paraxial optical system of focal length f. In this instance, a cancellation of quadratic phase terms occurs, and therefore the complex amplitude of the point-spread function, PSF_{ca} (or amplitude-spread function), is the Fourier transform of the complex pupil $\mathbf{A}$. For now, consider only one-dimensional (1-D) coordinate dependence in the pupil, and let $A(x)$ denote the aperture function. The following notation is used: $k = 2\pi/\lambda$, $i^2 = -1$, m is the "aberration" amplitude, a is the defocus parameter, and x is the pupil coordinate as shown in Fig. 2. The PSF_{ca} is expressed as

$$PSF_{ca} = \mathcal{F}(\mathbf{A}) = \mathcal{F}(A(x)\exp\{ik[ax^2 + m\sin(2\pi\nu_0 x)]\}).$$
$$(1)$$

Assuming that $km \ll 1$, the pupil function is then approximated by
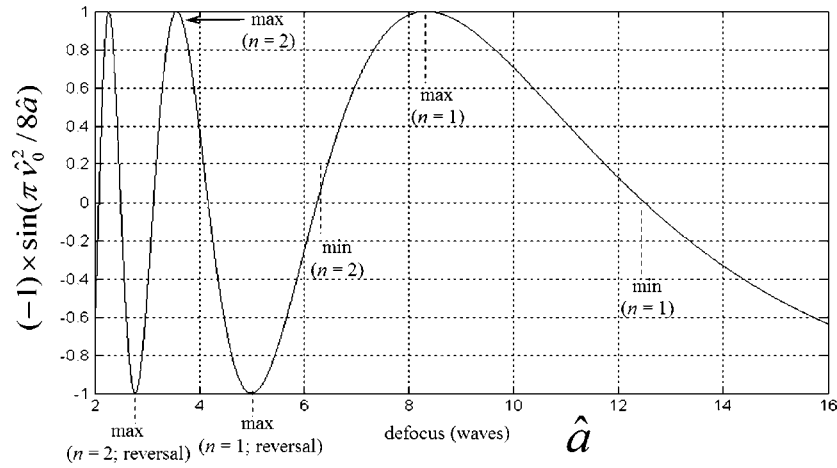
Fig. 3.   Plot of $\sin(\pi\hat{\nu}_0^2/8\hat{a})$ versus defocus for $\nu_0 = 10$ cycles/aperture.

$$\mathbf{A} \approx [1 + imk \sin(2\pi\nu_0 x)]A(x)\exp(ikax^2), \qquad (2)$$

so that Eq. (1) becomes

$$\mathrm{PSF}_{\mathrm{ca}}(\nu) = \mathcal{F}\{[1 + imk \sin(2\pi\nu_0 x)]\}$$
$$\otimes \; \mathcal{F}[\exp(ikax^2)] \otimes \mathcal{F}[A(x)], \qquad (3)$$

where $\otimes$ denotes convolution and $\mathcal{F}(\cdot)$ is the Fourier transform operator. Note from Eq. (3) that the Fourier transform of the aperture function acts simply as an over-all "modulator" of the result, i.e., the multiplier term $\mathcal{F}[A(x)]$ exhibits no functional dependence on ν_0, typically given by the Airy function for a circular aperture. Therefore, only the first two terms in Eq. (3) determine the condition for maximum and minimum contrast as a function of spatial frequency and defocus. With this observation, we leave the aperture geometry arbitrary in Eq. (3) and drop the $\mathcal{F}[A(x)]$ term for now. The consequences for neglecting the aperture will be discussed further in Section 5. Equation (3) then becomes ($\hat{\nu} \equiv x/\lambda f_{\#}$ is a dimensionless image plane spatial-frequency coordinate and $f_{\#}$ denotes f-number)

$$\mathrm{PSF}_{\mathrm{ca}} = \mathcal{F}(\mathbf{A})$$
$$= \left\{ \delta(\hat{\nu}) + \frac{mk}{2}[\delta(\hat{\nu} + \hat{\nu}_0) - \delta(\hat{\nu} - \hat{\nu}_0)] \right\}$$
$$\otimes \exp(-i\pi\lambda\hat{\nu}^2/2a), \qquad (4)$$

which further simplifies to

$$\mathrm{PSF}_{\mathrm{ca}} = \frac{1}{2}\left(\exp\left(\frac{-i\pi\lambda}{2a}\nu^2 \right) \right.$$
$$+ \frac{mk}{2}\left\{ \exp\left[\frac{-i\pi\lambda}{2a}(\nu + \nu_0)^2 \right] \right.$$
$$\left. \left. - \exp\left[\frac{-i\pi\lambda}{2a}(\nu - \nu_0)^2 \right] \right\} \right). \qquad (5)$$

Equation (5) takes a more convenient form when expressed in terms of the defocus parameter $\hat{a}$ (waves/radian), defined by first noting that

$$(a/\lambda)x^2 \to \hat{a}\hat{x}^2 = \frac{\hat{a}x^2}{(D/2)^2} \Rightarrow a = \frac{4\lambda}{D^2}\hat{a}, \qquad (6)$$

where $D/2$ is the aperture radius and the normalized pupil coordinate is $\hat{x} \equiv 2x/D$. In terms of the dimensionless variable $\hat{\nu}_0 = D\nu_0$ (cycles/aperture), the complex amplitude of the PSF is expressed finally as

$$\mathrm{PSF}_{\mathrm{ca}} = \frac{1}{2}\left(\exp\left(\frac{-i\pi}{8\hat{a}}\hat{\nu}^2 \right) + \frac{mk}{2}\left\{ \exp\left[\frac{-i\pi}{8\hat{a}}(\hat{\nu} + \hat{\nu}_0)^2 \right] \right. \right.$$
$$\left. \left. - \exp\left[\frac{-i\pi}{8\hat{a}}(\hat{\nu} - \hat{\nu}_0)^2 \right] \right\} \right). \qquad (7)$$

The intensity is the complex-conjugate square of Eq. (7). Given that $mk \ll 1$, the result simplifies to

$$I(\hat{\nu}) = \mathrm{PSF}_{\mathrm{ca}} \times \overline{\mathrm{PSF}_{\mathrm{ca}}}$$
$$= 1 - 2mk \sin(\pi\hat{\nu}_0^2/8\hat{a})\sin[2\pi(\hat{\nu}_0/8\hat{a})\hat{\nu}], \qquad (8)$$

again noting that diffraction due to the aperture stop has been ignored in this portion of the calculation. The effects due to the aperture stop are discussed further in Section 5 and illustrated numerically in Section 6.

3.   OPTIMAL DIVERSITY DEFOCUS

Considering the $\sin(\pi\hat{\nu}_0^2/8\hat{a})$ term of Eq. (8), the condition for maximum contrast in $\hat{\nu}_0$ as a function of defocus follows from

$$\frac{\pi\hat{\nu}_0^2}{8\hat{a}} = \frac{\pi}{2}(2n \pm 1) \Rightarrow \hat{a}_{\max} = \pm\frac{\hat{\nu}_0^2}{4(2n \mp 1)},$$
$$n = 0, 1, 2,..., \quad (9)$$

since

$$\sin\left[\frac{\pi}{2}(2n \pm 1) \right] = \mp\cos(n\pi), \qquad n = 0, 1, 2,... . \qquad (10)$$

That is, for a particular phase grating frequency $\hat{\nu}_0$, there exists a discrete set of defocus locations $\hat{a}_{\max}$ at which fringe contrast will be maximum. For example, the val-

ues of $\sin(\pi\hat{\nu}_0^2/8\hat{a})$ are plotted in Fig. 3 as a function of defocus for the numerical example of $\nu_0 = 10$ cycles/aperture. Heuristically, wavefront-sensing accuracy for $\hat{\nu}_0$ is expected to be greatest at these diversity values.

A couple of comments should be made with regard to Eq. (9). For $n \gg 1$, the predicted optimal defocus values tend toward zero. However, in practice, zero defocus results in zero contrast for $\hat{\nu}_0$. This behavior is indicated in Fig. 3, where we note that as $\hat{a} \to 0$ the frequency of oscillation of the $\sin(\pi\nu_0^2/8\hat{a})$ term approaches infinity, and therefore the contrast differences between various maxima and minima are not resolved, i.e., the ± 1 diffraction orders will fall within the Airy disk, yielding a zero fringe contrast. Second, the analysis that we have presented is based on the assumption that the PSF is treated as a continuous function, i.e., measured with a perfect detector with continuous sampling. This assumption neglects the fact that in practice the PSF is sampled over a finite grid (a detector array). As a result, nonzero defocus values are preferred when the PSF data are undersampled over a finite grid, despite the prediction of Eq. (9). That is the primary reason for including a nonzero defocus value is to "spread out" the PSF response to such a degree as to indicate how the aberrations are modulating the intensity data. A detailed study of sampling effects is beyond the scope of this paper and will be considered in a future analysis.

The + sign in the *denominator* of Eq. (9) represents a contrast reversal in the spectral power with respect to the signal contrast predicted by the negative-sign case. Both cases yield a maximum in the signal $\hat{\nu}_0$ and originate from the $\mp$ sign in Eq. (10). Therefore we make no distinction between these two cases insofar as wavefront sensing is concerned. The $\pm$ sign preceding Eq. (9) [and Eq. (11) below] is independent of the $\mp$ sign in Eq. (10) and shows that maximum contrast is obtained for equally spaced defocus values placed on either side of the image plane by inspection of Eq. (8). The implication for wavefront sensing is that a diversity image can be placed on either side of focus, while still maintaining maximum contrast in $\hat{\nu}_0$ according to Eq. (9). This result has been obtained independently from an earlier Cramér–Rao analysis.[22] General consistency between the Cramér–

Rao analysis and the results above are considered further in Section 7.

A basic observation from Eq. (9) is that $\hat{a}_{\max}$ increases quadratically with $\hat{\nu}_0$. Therefore, to the extent that estimating $\hat{\nu}_0$ is aided by stronger spectral power in the data, the recovery of higher-spatial-frequency aberration signals will generally benefit from larger defocus values. This interpretation is supported in Section 7 [see relation (21)] by an estimation-theoretic analysis. Conversely, it follows that lower-spatial-frequency aberrations will generally benefit from smaller, diversity defocus settings. The wavefront-sensing implications are discussed further in Section 8. Referring again to Eq. (8), minima in the spectral power occur when

$$\frac{\pi\hat{\nu}_0^2}{8\hat{a}} = n\pi \Rightarrow \hat{a}_{\min} = \pm\frac{\hat{\nu}_0^2}{8n}, \qquad n = 0, 1, 2,.... \ (11)$$

The predictions for maximum or minimum contrast were derived assuming a 1-D pupil function but are also valid for the two-dimensional (2-D) case, since spatial frequencies in orthogonal directions separate as convolution products by inspection of Eqs. (2) and (3). As a consistency check, several defocus values are calculated from the predictions for the maxima and the minima and then compared with their 2-D numerical counterparts by means of fast Fourier transforms (FFTs). These comparisons are made in Section 6.

4. MAXIMUM DIVERSITY DEFOCUS

In addition to the contrast maxima and minima that occur (e.g., Fig. 3), a theoretical value of maximum diversity defocus exists, beyond which there is a penalty in imaging contrast for further increasing focus. This value corresponds to the last contrast reversal/maxima, $n = 0$, in Eq. (9),

$$\hat{a}_{\text{rev,max}} = \pm\frac{\hat{\nu}_0^2}{4}, \tag{12}$$
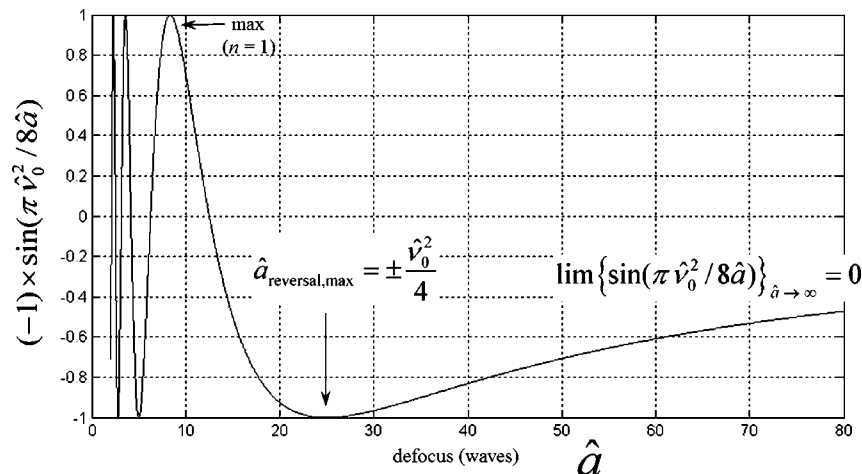
and in the limit as $\hat{a} \to \infty$,

Fig. 4. Position of maximum diversity defocus for $\nu_0 = 10$ cycles/aperture.

$$\lim_{\hat{a} \to \infty} \{\sin(\pi \hat{\nu}_0^2/8\hat{a})\} = 0, \qquad (13)$$

corresponding to a contrast minimum. Therefore, arbitrarily increasing the magnitude of diversity defocus beyond the value predicted by Eq. (12) can only hinder wavefront-sensing performance. Alternatively, the limit in Eq. (13) is consistent with a contrast minimum at the defocus value of infinity, corresponding to $n = 0$ in Eq. (11). A specific numerical example is illustrated in Fig. 4.

The existence of a maximum value for diversity defocus is consistent with earlier Cramér–Rao studies of quadratic curvature wavefront sensing,[4] but for a different reason. In Ref. 4, this effect is attributed to the optical transfer function (OTF) developing zeros as defocus is increased, leading to a reduction in contrast at the focal plane. But the present analysis shows that for aberration recovery through phase retrieval, the penalty in imaging contrast is due to the fact that information on $\hat{\nu}_0$ is shifted to "dc" in the image as $\hat{a} \to \infty$. Furthermore, "windows" of spectral power corresponding to $\hat{\nu}_0$ are shown to exist at the defocus values predicted by Eq. (9). The locations of these windows in the spectral power are calculated from the OTF in Section 6.

5. ROLE OF APERTURE GEOMETRY AND TALBOT IMAGING

By inspection of Eqs. (8) and (11), the minimum-contrast case corresponds to the intensity value

$$I_{\min} = 1, \qquad (14)$$

implying that the minimum-contrast case contains no information on the signal $\hat{\nu}_0$ when aperture geometry is neglected. As expected, the corresponding Cramér–Rao bound is infinite, as shown in Section 7 [see Eq. (22)]. This result not only identifies the estimation-theoretic consequence of neglecting aperture geometry but also emphasizes the fundamental role played by diffraction in the recovery of aberration information from intensity data. In Section 6, comparisons are made between the analytical predictions above [Eqs. (9) and (11)] and their 2-D numerical counterparts by means of FFTs. In particular, a visual inspection of the minimum-contrast result in Fig. 6 below indicates that spatial-frequency information corresponding to $\hat{\nu}_0$ is "dispersed" at the aperture boundary because of diffraction by the aperture stop. Indeed, it is this diffracted "information" due to the aperture response that allows the recovery of $\hat{\nu}_0$ from the minimum-contrast intensity data, as illustrated in Fig. 8 below.

The Talbot imaging phenomena[23] consist of periodic "self-images" formed by an amplitude grating under coherent illumination in the Fresnel zone. The grating behaves as an image-forming system or "lens" as a result of interference that results from the diffractive nature of the grating. An important corollary result is that the Fresnel zone propagation of spectral power is mathematically equivalent to the Fraunhofer propagation of a defocused pupil plane. This is due to the quadratic phase factors carried in each case. In Section 3, we have shown that a defocused phase grating yields an imaging phenomenon completely analogous to Talbot imaging, but for a phase grating rather than an amplitude grating. The locations of the "Talbot" image planes are thus marked by regions of maximum and minimum contrast as a function of spatial frequency as well as contrast reversal in the spectral power. The locations of the maxima and the contrast reversals give predictions for the optimal diversity defocus values for wavefront sensing, as demonstrated in Section 8.

6. OPTICAL TRANSFER FUNCTION

The (incoherent) optical transfer function (OTF) is defined as the Fourier transform of the PSF (or, equivalently, the autocorrelation of the pupil). Therefore, using Eq. (8), we calculate the OTF as a function of spatial frequency and defocus:

$$
\begin{aligned}
\text{OTF}(\hat{\omega}) &= \mathcal{F}[I(\hat{\nu})] \\
&= \delta(\hat{\omega}) + imk \sin(\pi \hat{\nu}_0^2/8\hat{a}) \\
&\quad \times [\delta(\hat{\omega} - \hat{\omega}_0) - \delta(\hat{\omega} + \hat{\omega}_0)], \qquad (15)
\end{aligned}
$$

where δ is the Kronecker delta function and ω_c is the incoherent cutoff frequency, given in

$$\hat{\omega} = \lambda f_\# \omega = \omega/\omega_c, \qquad (16)$$

with $\hat{\omega}_0$ defined as

$$\hat{\omega}_0 \equiv \hat{\nu}_0/8\hat{a}. \qquad (17)$$

Equation (17) is the main result, locating "windows" of the OTF peak response as a function of spatial frequency and defocus. The result in Eq. (15) is idealized in the sense that the locations of peak response are marked by delta functions, but when aperture geometry is included, the delta functions are replaced by a "finite-spread" function because of the aperture response. This effect is illustrated in Fig. 5, which gives a graphical comparison of the analytical prediction [Eq. (17)] with the corresponding 2-D numerical OTF calculation. The calculation assumes an unobscured circular aperture and propagation with FFTs. The same comparison is repeated in Fig. 6 for the minimum-contrast case.

Typical numerical values for the various contrast cases are listed in Table 1 for $\nu_0 = 10$ cycles/aperture. The values follow from Eqs. (9) and (11), using $n = 0, 1, 2$. The $+$ and $-$ subscripts in the maximum-contrast cases distinguish between the $+$ and $-$ signs in the denominator of Eq. (9) (i.e., the $+$ case is a contrast reversal): As pointed out above, Figs. 5 and 6 give a graphical comparison of the analytical predictions (for $n = 1$), as listed in Table 1, and their 2-D numerical counterparts. The $+$ case (a contrast reversal) is omitted, since it is nearly identical to the contrast maxima, aside from a $\pi/2$ phase shift in the "band" structure of the defocused intensity data. For simplicity, an unobscured circular aperture is assumed as well as 512×512 Nyquist-sampled PSFs. As noted earlier in Section 3, information on the signal $\hat{\nu}_0$ is shifted to dc in the image as defocus is increased beyond the theoretical value predicted in Eq. (12). This result is corroborated by the OTF calculation above [and by the Cramér–Rao bound below—see the comments after
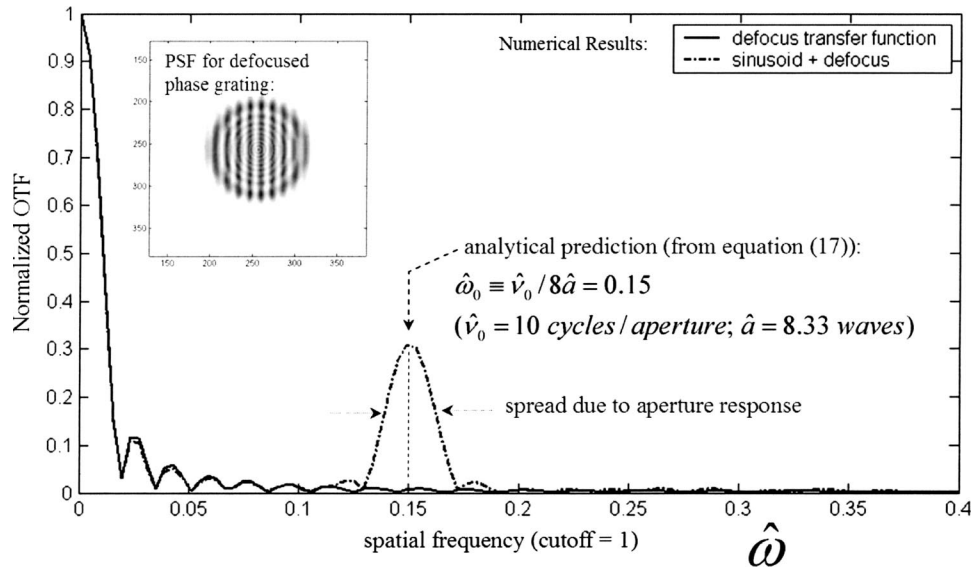
Fig. 5.   Comparison of transfer functions and analytical prediction for contrast maxima for $n = 1$ and $\nu_0 = 10$ cycles/aperture; defocus = 8.33 waves.
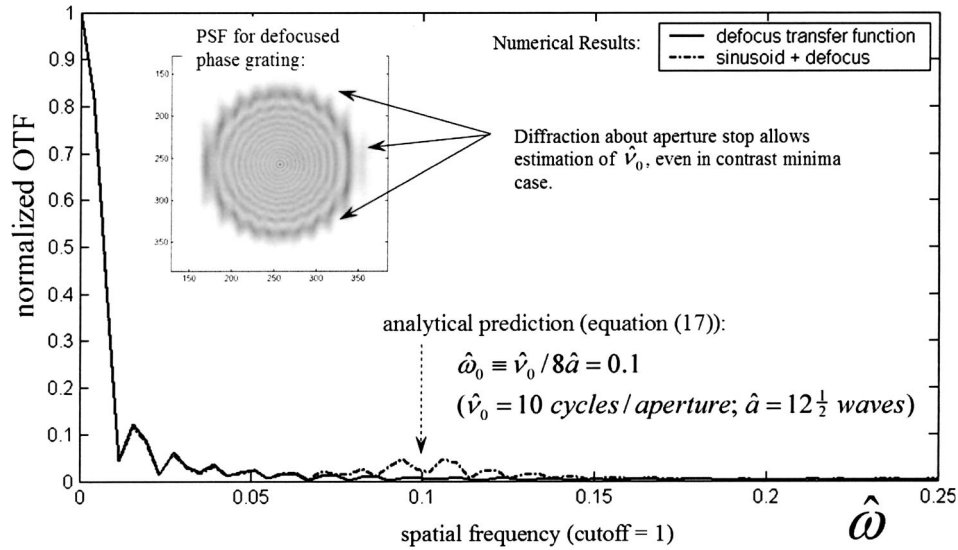

Fig. 6.   Comparison of transfer functions and analytical prediction for contrast minima for $n = 1$ and $\nu_0 = 10$ cycles/aperture; defocus = 12.5 waves.

relation (21)], since $\hat{\omega}_0 \rightarrow 0$ as $\hat{a} \rightarrow \infty$ in Eq. (17), i.e., $\hat{\omega}_0$ decreases toward the dc component of the transfer function.

7. CONSISTENCY WITH THE CRAMÉR–RAO LOWER BOUND

The Cramér–Rao lower bound is calculated from a statistical model relating the parameters being estimated to noise in the measured data. As a result, the calculation provides the basis for a physical understanding of how estimation errors are affected by signal-to-noise ratio, diversity functions, sampling, and so on. In this section, the Cramér–Rao theorem is briefly reviewed, and its application to focus-diverse wavefront sensing is discussed. We then demonstrate consistency between the Cramér–Rao bound and the analytical results of Section 3.

Table 1.   Summary of Defocus Values Corresponding to Contrast Maxima and Minima for $n = 0, 1, 2$, Assuming $\hat{\nu}_0 = 10$ Cycles/Aperture

n	$|\hat{a}_{\max(-)}|$ (waves)	$|\hat{a}_{\max(+)}|$ (waves)	$|\hat{a}_{\min}|$ (waves)
0	25.0	25.0	∞
1	8.33	5	12.5
2	3.57	2.78	6.25

The statistical model is given by the Poisson probability density function for photon-limited images. The Fisher information array for phase-diverse imaging is defined as the negative expectation of the log-likelihood Hessian matrix (Refs. 5 and 24):

$$F_{\alpha\beta} \equiv -E(\partial^2_{\alpha\beta}L) = N_p \sum_{m=1}^{M} \sum_{i,j} (\partial_\alpha \mathrm{PSF}_m)(\partial_\beta \mathrm{PSF}_m)/\mathrm{PSF},$$

(18)

where $\partial_\alpha \equiv \partial/\partial a_\alpha$, $\partial^2_{\alpha\beta} \equiv \partial^2/\partial a_\alpha \partial a_\beta$, the a_β are the aberration coefficients, the (i, j) refer to pixel samples, L is the log-likelihood function, and $E(\,\cdot\,)$ denotes ensemble average over a statistically meaningful distribution of aberrations. In Eq. (18), the Fisher array has been normalized to the total photon count $N_p = \Sigma_{(i, j)}\text{PSF}$, and M is the total number of diversity channels.

The Cramér–Rao theorem[6] states that

$$\text{Var}(\hat{a}_\beta) \equiv \sigma^2_{a_\beta} \geqslant F^{-1}_{\beta\beta}(\mathbf{a}), \qquad (19)$$

where $\text{Var}(\cdot)$ is the variance, F^{-1} is the inverse of the Fisher array, and $\hat{a}_\beta$ denotes an unbiased estimator for the βth aberration parameter. An intuitive understanding of the Cramér–Rao theorem is obtained by inspection of Eq. (18) [and Eq. (19)]: The error bounds in estimation performance are inversely proportional to the expected "curvature" of the log-likelihood function L, that is, to the sensitivity of L on the parameters being estimated. Therefore it will be easier to produce more accurate estimates from data sets in which L is strongly influenced by the parameters that we wish to estimate. Conversely, for data corrupted by noise and other degrading factors, the functional dependence on the parameters will be reduced, and therefore the bounds will be correspondingly higher. This theoretical framework indicates that a study of the propagation of spectral power associated with aberration "signals" can be used to identify optimal recovery configurations as a function of the aberration spatial frequency and provides a quantitative basis in estimation theory for the results in this paper.

Substituting Eq. (8) into Eq. (18) gives a simple consistency check on the above interpretation. Note, however, that this calculation is not really the Cramér–Rao bound, since the statistical interpretation has been ignored [by assuming a single aberration realization, i.e., a $\sin(\cdot)$ phase term]. Nevertheless, given that the bound is inversely proportional to the gradient of the PSF with respect to the aberration parameter being estimated, the calculation gives an accurate indicator of how the Cramér–Rao bound will behave analytically as a function of spatial frequency and defocus. The partial derivative of Eq. (18) is thus calculated, and the Fisher information has the following proportionality relation:

$$F \propto (\partial_\nu I)^2|_{\hat\nu \to \hat\nu_0} = [km\pi\hat\nu_0 \cos(\pi\hat\nu^2_0/4\hat{a})\sin(\pi\hat\nu^2_0/8\hat{a})/2\hat{a}]^2. \qquad (20)$$

The presence of the $\sin(\pi\hat\nu^2_0/8\hat{a})$ term in relation (20) shows that the contrast maxima and minima are identical to the earlier predictions derived in Section 3 but are derived independently based on the propagation of spectral power for a defocused phase grating. Numerical correspondence is illustrated in Fig. 7 as a function of defocus, assuming, as above, that $\hat\nu_0 = 10$ cycles/aperture for a single diversity channel. Hence the predictions for optimal contrast based on the propagation of spectral power are consistent with the estimation-theoretic lower bound (compare Figs. 3 and 4 with Fig. 7). In Fig. 7, a variety of higher-order maxima begin to dominate as $\hat{a} \to 0$ because of the $1/\hat{a}^2$ dependence of the gradient and the fact that sampling effects have been ignored, as pointed out earlier in the discussion following Eq. (10). A proper math-

ematical analysis of sampling effects will introduce appropriate deweighting factors for smaller defocus, reducing the relative magnitudes predicted by relation (20), the analysis of which is beyond the scope of this paper.

The Fisher information corresponding to the maximum-contrast case is calculated by substituting $\hat{a}_{\max}$ into relation (20) to get

$$F_{\max} \propto \left[\frac{2km(1 - 4n)}{\hat\nu_0}\right]^2. \qquad (21)$$

For a fixed numerator in relation (21), the $1/\hat\nu_0$ dependence implies that the estimation problem becomes more difficult as $\hat\nu_0$ increases. By inspection of the result in relation (20), this result is simply an alternative statement of the fact that the spectral content of $\hat\nu_0$ is shifted to dc in the image as $\hat{a} \to \infty$. Finally, the minimum-contrast case yields

$$F_{\min} = 0, \qquad (22)$$

and therefore the Cramér–Rao bound is infinite, consistent with the earlier result in Eq. (14), since no information on $\hat\nu_0$ is present when aperture geometry is neglected.

8. WAVEFRONT-SENSING IMPLICATIONS

The presence (or the absence) of $\hat\nu_0$ in the PSF intensity data is striking upon comparison of the maximum and minimum-contrast cases of Figs. 5 and 6 and indicates the potential benefits of properly matching diversity defocus values to the desired spatial frequency of recovery. As expected, there are wavefront-sensing implications as well. Here we consider several simulations to investigate the wavefront recovery performance for a focus-diverse iterative-transform phase-retrieval algorithm as defocus and spatial frequency are varied. Although we have not attempted to advocate any one algorithmic approach in this paper, the iterative-transform (or point-by-point phase-recovery) method is in fact especially suited for our discussion of mid-spatial-frequency aberrations. Indeed, the recovery of mid to high spatial frequencies utilizing the parametric approach is impractical given that such parameterized formulations require solving for thousands of aberration basis coefficients, as indicated in the fitting results of Fig. 17 below.

The core algorithm is based on the Gerchberg–Saxton[25] iterative-transform method, as discussed by Misell.[26] Roddier and Roddier[27] utilized this method for analyzing the Hubble PSFs and have discussed additional details of it in Ref. 28. The algorithm has also been utilized by Fienup et al.,[29] and Lyon has conducted a detailed simulation study of the algorithm.[30] This approach has been utilized by Redding et al.,[31,32] as the baseline wavefront-sensing method for NASA's Next Generation Space Telescope (subsequently named the James Webb Space Telescope). A bandpass sensitivity analysis has been discussed in Refs. 13 and 33. Other phase-retrieval methods have also been discussed in the literature based on the transport of intensity (e.g., Ref. 34).

The first simulation addresses the recovery of a single pupil spatial-frequency component $\hat\nu_0$, i.e., a sinusoid ab-
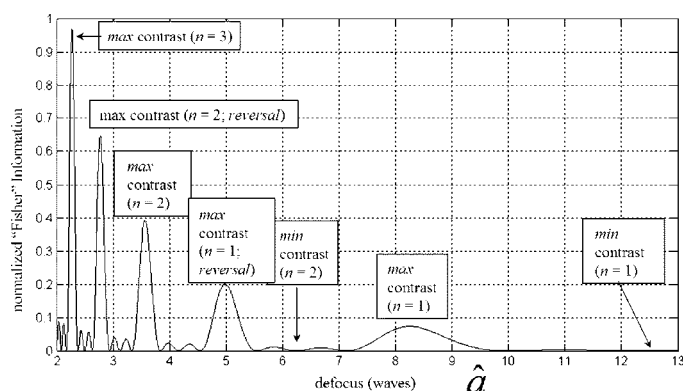
Fig. 7.   Fisher information versus defocus for a phase grating assuming $\nu_0 = 10$ cycles/aperture.   Values predicted by Eqs. (9) and (11) are also identified.
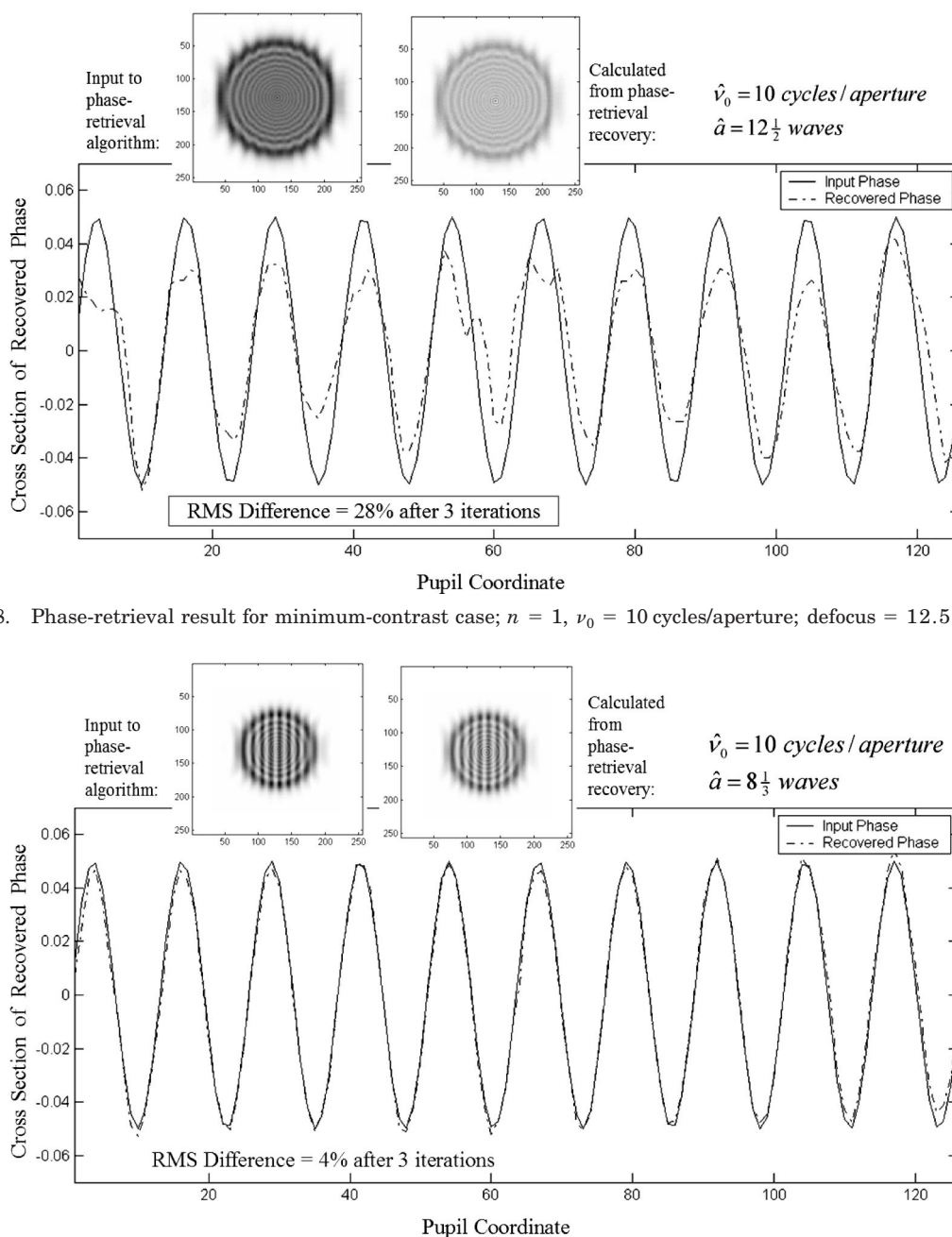

Fig. 8.   Phase-retrieval result for minimum-contrast case; $n = 1$, $\nu_0 = 10$ cycles/aperture; defocus = 12.5 waves.
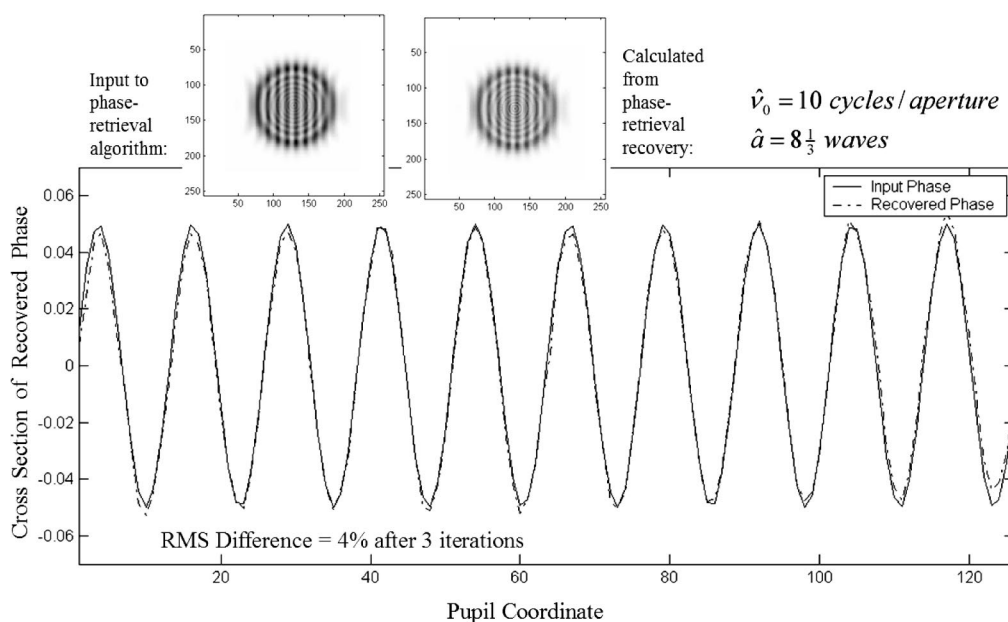

Fig. 9.   Phase-retrieval result for maximum-contrast case; $n = 1$, $\nu_0 = 10$ cycles/aperture; defocus = 8.33 waves.
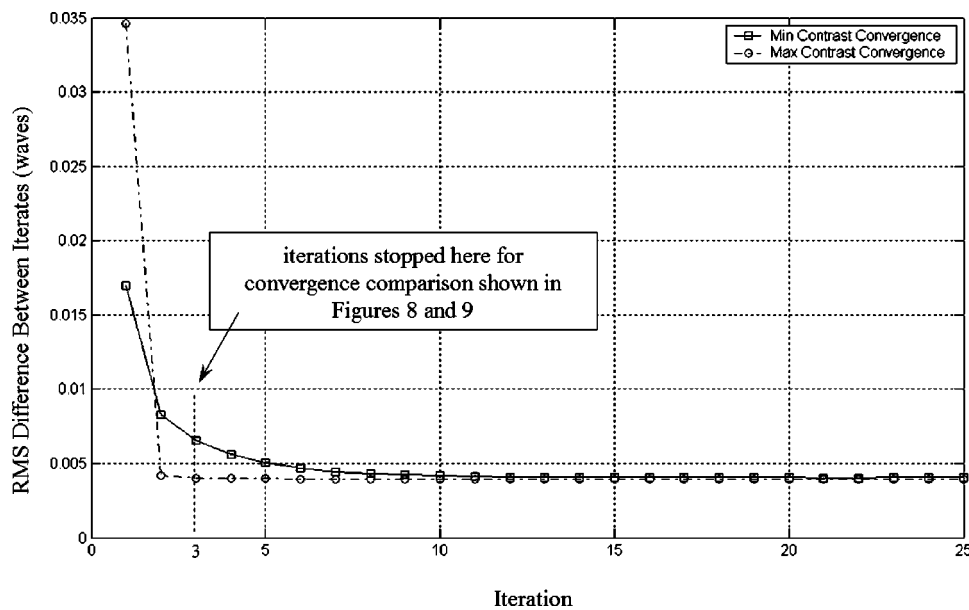
Fig. 10.   Phase-retrieval convergence comparison for maximum- and minimum-contrast cases.

erration as a function of defocus. Two additional simula-
tions are then considered to examine wavefront-sensing
performance for aberrations having more complicated
spatial-frequency dependence. In the first instance, a
low-order optical aberration is introduced to demonstrate
the advantage of utilizing a smaller diversity defocus
value.   In the second, the higher-spatial-frequency
"print-through" associated with a deformable mirror is ex-
amined to address an instance where larger diversity de-
focus values can be advantageous to wavefront-sensing
accuracy. As an example of this type of mid-spatial-
frequency recovery, we routinely perform such phase re-
trievals on the NASA Goddard wave-front-control testbed
to register actuators and to flatten the wavefront to ap-
proximately $\lambda/40$ rms.   In this instance, m of relation (2)
is approximately 3/40 (and $km < 1$), consistent with the
interferometer data discussed in Ref. 35.

For simplicity, monochromatic Nyquist-sampled PSFs
are generated for the simulations. Additive noise, detec-
tor quantization effects, and blurring functions such as
jitter and charge diffusion are neglected, since it is ex-
pected that some bias (estimation bias for the Misell–
Gerchberg–Saxton algorithm has been discussed in Ref.
36) will be introduced into the aberration estimate due to
these external effects alone. The analysis of estimation
bias in image-based wavefront sensing as a function of
PSF blurring functions is beyond the scope of this paper,
since the sensitivity to these factors is expected to be al-
gorithm and perhaps implementation dependent. Hence
we consider only a single algorithm implementation (the
authors'), as discussed above, to demonstrate the main
points of the paper.

The first simulation begins with the calculation of two
symmetrically placed defocused PSFs for input to a modi-
fied Misell–Gerchberg–Saxton estimation procedure.
For convenience, the numerical value $\hat{\nu}_0 = 10$ cycles/
aperture is selected, and then the diversity defocus values
are derived according to Eqs. (9) and (11), respectively.
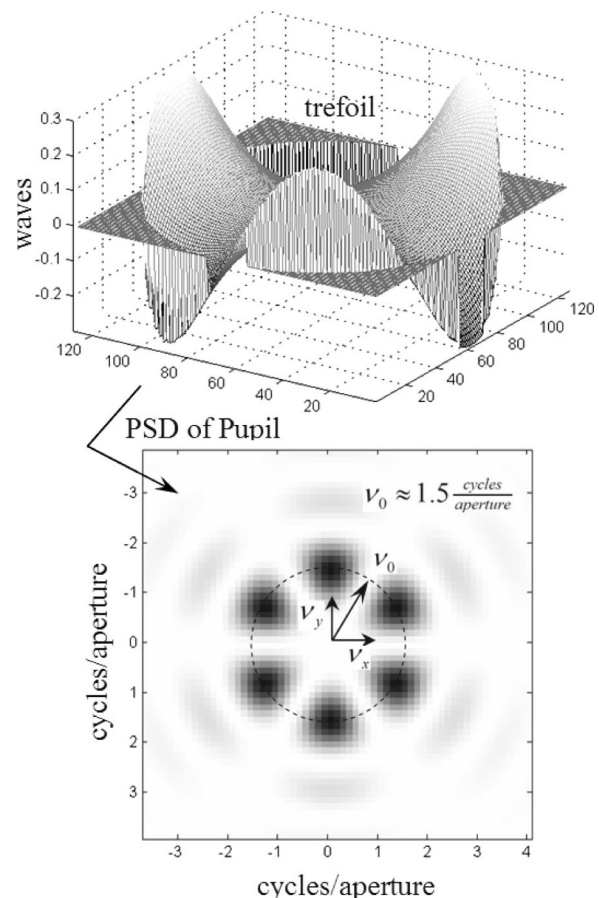The minimum-contrast wavefront-sensing result is shown

Fig. 11.   Trefoil power spectral density (PSD).

in Fig. 8, while the maximum-contrast case is given for
comparison in Fig. 9.   In each case, the algorithm is ex-
ecuted for an identical (fixed) number of iterations and
then terminated.   After only three iterations, the
maximum-contrast phase-retrieval estimate has nearly

converged to the correct value with an rms error of approximately 4%, while the minimal-contrast case converges at a much slower rate, with an rms error of approximately 28%. The convergence is plotted in Fig. 10, showing the rms difference between individual iterates as a function of the number of iterations. After 25 iterations; the algorithm converges (in each case) to an rms difference between iterates of approximately $\lambda/250$. The
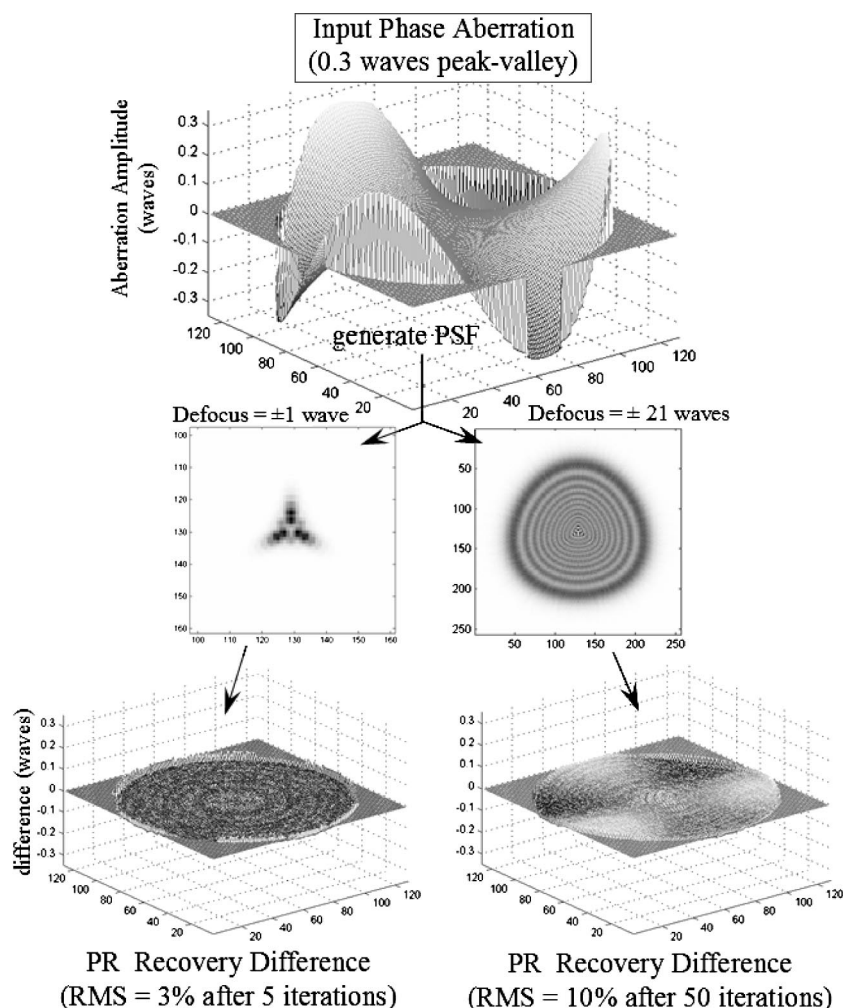

Fig. 12.   Diversity point-spread function (PSF) data and phase-retrieval (PR) results for the trefoil aberration.
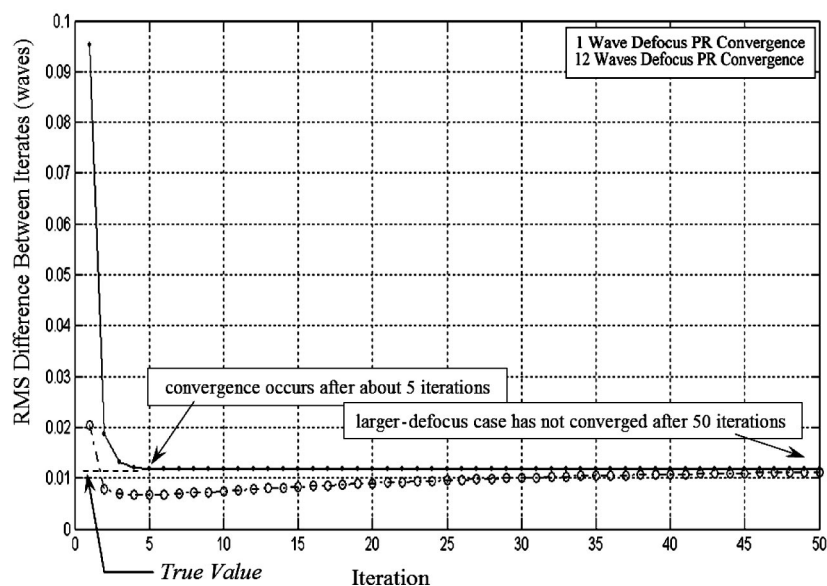

Fig. 13.   Phase-retrieval convergence comparison for phase-retrieval results shown in Fig. 12.

Deformable Mirror
Actuator "print-through"

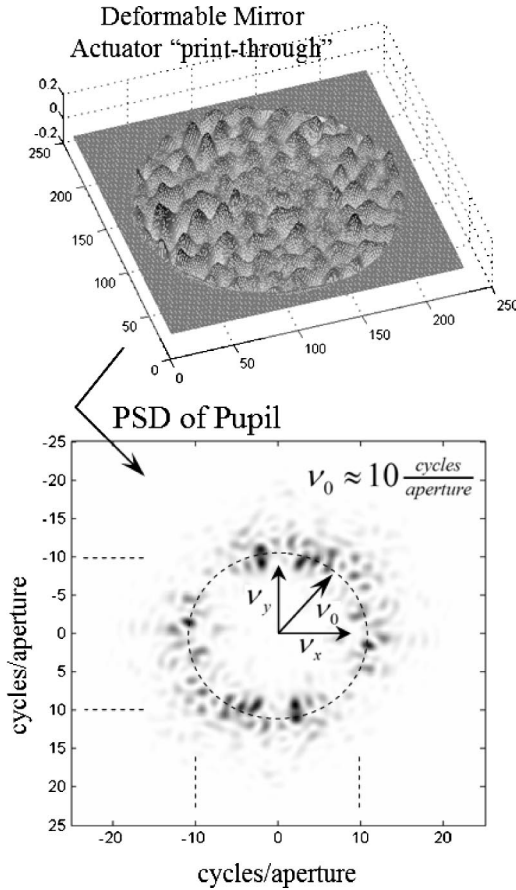PSD of Pupil

$$\nu_0 \approx 10 \frac{cycles}{aperture}$$

Fig. 14.   Deformable mirror "print-through" PSD.

final estimate for the maximum-contrast phase-retrieval result differs by only approximately 3% from the true phase value, while the minimum-contrast estimate differs by 10%. Additional discussion is given in Section 10.

The second simulation compares the estimation performance between the maximum- and minimum-contrast diversity cases for a phase error of lower spatial frequency. The trefoil aberration is arbitrarily selected (Zernike order 4, term 7 out of 15 terms in the Malacara ordering[37]), which is approximated by a sinusoidal spatial-frequency component of approximately $\hat{\nu}_0 = 1.5$ cycles/aperture, as illustrated by the power spectral density (PSD) calculation shown in Fig. 11 (diversity defocus values implied by a given spatial frequency are derived from the Zernike basis order in Section 9). In this instance, Eq. (9) predicts a maximum-contrast defocus value of approximately $a_{max} \approx \pm 1$ wave for $n = 0$. The first image of the input data (a symmetrically placed diversity pair) to the phase-retrieval algorithm is shown in Fig. 12, where we note that the larger-defocus pair was generated for a somewhat arbitrarily selected ±12 waves, since $a_{min} \to \infty$ for $n = 0$ (i.e., spectral power shifts to dc in the image, as noted earlier in Section 6).

The phase-retrieval algorithm discussed earlier recovers a point-by-point phase map, which in turn is subsequently decomposed into a Zernike basis set. By inspection of Fig. 12, one can easily see the trefoil content strongly modulating the smaller-defocus PSF. But in the larger-defocus case, the trefoil is barely visible. The

rms difference between the input and recovered phases is also shown in Fig. 12, where we note that for a fixed number of iterations (50 in this instance), the smaller defocus data yield a better result when measured in terms of algorithm convergence. The wavefront-sensing convergence is plotted in Fig. 13, showing the rms difference between individual phase-retrieval iterates. Compared with the purely sinusoidal result of Fig. 10, the difference in phase-retrieval convergence between the two cases is slightly slower. This is likely due to the more complicated spatial-frequency dependence of the trefoil aberration compared with that of a pure sinusoid. Nevertheless, the smaller-defocus case converges after approximately five iterations, while the larger-defocus case has not converged after 50 iterations, as indicated by the presence of trefoil in the phase residual difference of Fig. 12.

Finally, consider the case of a mid-spatial-frequency phase error (ripple) such as that produced by a deformable mirror. The phase residual used for generating the PSFs was obtained from a Zygo interferometer data set after flattening a Xinetics 349 channel deformable mirror, as discussed in Ref. 35. The Xinetics deformable mirror has 21 actuators along the maximum x and y pupil directions, and therefore $\hat{\nu}_{0x} = \hat{\nu}_{0y}$ is approximately 10 cycles/aperture, as illustrated by the PSD calculation shown in Fig. 14. The optimal diversity defocus value for the maximum-contrast case is calculated by using Eq. (9) and listed in Table 1 for $n = 1$, giving $\hat{a}_{max} = \pm 8.33$. The smaller defocus value is chosen based on the minimum-contrast prediction using Eq. (11), giving $\hat{a}_{min} = \pm 2.5$ waves of defocus for $n = 5$. In this instance, one can easily see the actuator residuals in the defocused PSFs, but in the smaller-defocus case, the residual is not as clearly defined. Two sets of defocused PSFs (each consisting of a positive/negative defocus pair) were simulated and are shown in Fig. 15. Although phase-retrieval convergence is relatively quick in the smaller-defocus case, the final result is less accurate (biased) compared with that of the larger-defocus case, where we note that actuator residuals are still present in the difference between the starting and recovered phase aberrations for the smaller defocus data. Therefore, in this instance, we see that larger defocus can be advantageous for the recovery of higher-spatial-frequency phase aberrations based on accuracy. Additional discussion is given in Section 10.

9. DIVERSITY DEFOCUS IMPLIED BY THE ZERNIKE BASIS FUNCTIONS

In this section, a statistical calculation of the frequency content implied by the Zernike basis functions of a given order is considered (for convenience, we adopt the Malacara-ordered Zernike functions[37]). The calculation suggests a "target" aberration spatial-frequency content that one may match to a given Zernike order in units of cycles per aperture. Therefore, using Eq. (9), one can then calculate optimal diversity defocus values as a function of the desired spatial frequency of wavefront-sensing recovery, expressed in terms of a given Zernike polynomial order.
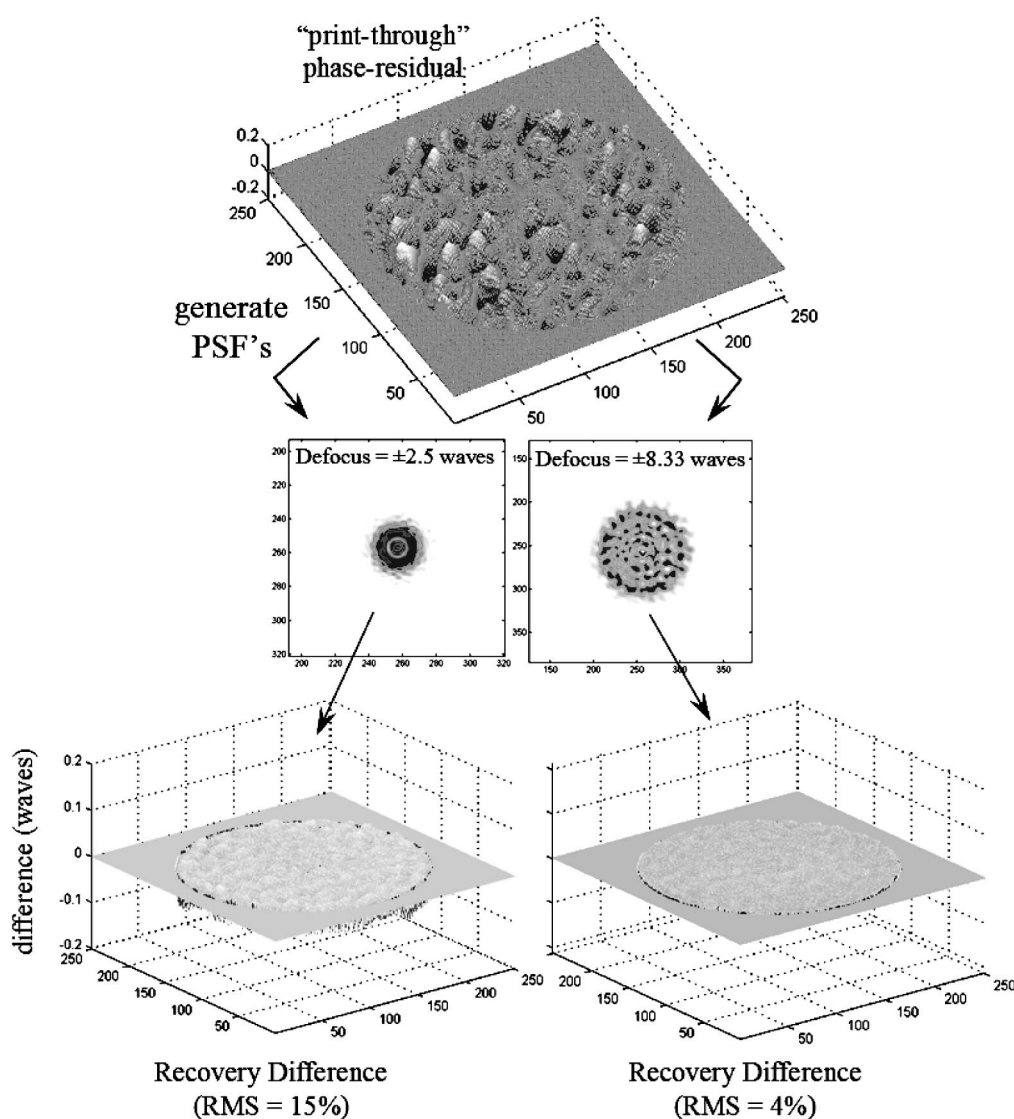
Fig. 15.   Diversity PSF data and phase-retrieval results for a deformable mirror "print-through" phase residual.

For convenience, we adopt an unobscured circular aperture and normalize the coefficients to peak–valley units. The mean PSD is calculated by first generating a number of aberration realizations for a given Zernike order N and then averaging the peak PSDs obtained in each case. This mean PSD value for a given Zernike order is intended to represent a target spatial frequency that can be represented in the Zernike basis of a given order. For simplicity, the $(N + 1)(N + 2)/2$ Zernike aberration coefficients for a given realization are taken from a Gaussian distribution. Similar aberration realizations have been discussed in Ref. 5 for calculation of the Cramér–Rao bounds. Analytical PSD calculations from the Zernike basis set have been discussed in Ref. 38.

The numerical results are summarized in Fig. 16, which plots the peak PSD (dominant spatial frequency) versus the Zernike order, from order 4 (15 terms) to order 12 (91 terms). Assuming a linear relationship between the peak PSD and the Zernike order allows one to extrapolate these results to higher orders by using a linear fit to the mean PSD values, as shown in Fig. 16:
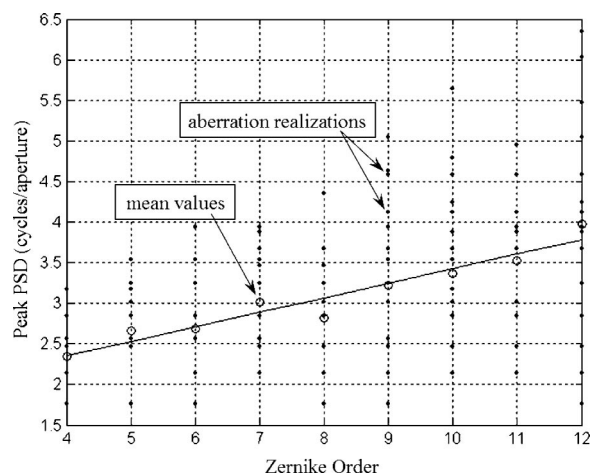

Fig. 16.   Dominant PSD versus Zernike order.

$$\mathrm{PSD}_{\mathrm{mean}} = b Z_{\mathrm{order}} + c,$$

$$b = 0.1787, \qquad c = 1.64 \ \mathrm{cycles/aperture}. \qquad (23)$$

Applying these results to the mid-spatial-frequency deformable mirror actuator residual shows that Zernike order 50 (1326 terms) is sufficient to represent approximately 10 cycles/aperture according to Eq. (23). However, it should be noted that these results depend solely on the assumed linearity of the PSD means of Fig. 16 through higher orders than 12. The standard deviation about these mean values is significant, and, therefore order-of-magnitude estimates are all that should be claimed from Eq. (23).

Of course, higher-order decompositions result in better approximations, but only up to a point. This limitation is due to the fact that higher-frequency noise or "spiky" phase data cannot be accurately represented by using a Zernike basis (or any other basis) for a fixed number of data values across the pupil. Once this limitation has been reached for a given phase map, the fit saturates, and then no significant improvement in the fitting is realized by increasing the order of the fit. This behavior is illustrated in Fig. 17, which plots the rms difference between the deformable mirror actuator residual and the Zernike fit to these data as a function of the Zernike fit order. The plot also gives a consistency check on the relationship implied by Eq. (23); e.g., at approximately Zernike order 45–50 (1081–1326 terms), the curve begins to level out to approximately $\lambda/100$ (rms fit error for 10 cycles/aperture) as the noise floor in the data is reached. A single data point is also illustrated in Fig. 17, showing the deformable mirror data, the Zernike fit to these data (e.g., order 50), and the difference between the fit and the data.

Finally, setting $\hat{\nu}_0 \equiv \mathrm{PSD}_{\mathrm{mean}}$ [i.e., substituting Eq. (23) into Eq. (9)] gives a prediction for the maximum-contrast diversity defocus values as a function of the desired spatial frequency of wavefront-sensing recovery, expressed in terms of a given Zernike polynomial order:

$$\hat{a}_{\max} = \pm(bZ_{\mathrm{order}} + c)^2/(16n \mp 4), \qquad n = 0, 1, 2, ..., \tag{24}$$

assuming the numerical values for b and c listed in Eq. (23). A similar expression is obtained upon substitution for the contrast minima, plotted in Fig. 18 for several values of $n = 0$ and 1.

10. SUMMARY AND DISCUSSION

The analysis that we have considered is based on the observation that pupil phase aberrations may be decomposed into different spatial-frequency regimes (low + mid + high) and that specific defocus values tend to emphasize (or minimize) spectral power corresponding to different spatial frequencies in the pupil. Therefore, to the extent that one can assume that an aberrated wavefront is composed of a dominant spatial frequency, one can use Eq. (9) to predict the defocus values corresponding to maximum contrast in the aberration signal. Conversely, Eq. (11) predicts diversity defocus values that should be avoided. As discussed in Section 5, this behavior is completely analogous to the Talbot imaging phenomena for a phase grating, explaining multiple periodic regions of maximum and minimum contrast as a function of spatial frequency and defocus.

Since image-based wavefront-sensing methods operate from intensity data, wavefront-sensing performance is therefore expected to vary as the spectral power corresponding to aberration spatial frequency varies with defocus. In Section 8, several simulations were conducted to indicate some details of this sensitivity. The three main pupil phase aberrations considered were (a) a pure sinusoidal frequency component, (b) a low-order optical phase error, and (c) a mid-spatial-frequency optical phase error. In (a), accelerated convergence is the dominant improvement obtained by properly matching diversity defocus. Although some deviation in accuracy exists for phase-retrieval results between the optimal and suboptimal diversity values, improved convergence is really the
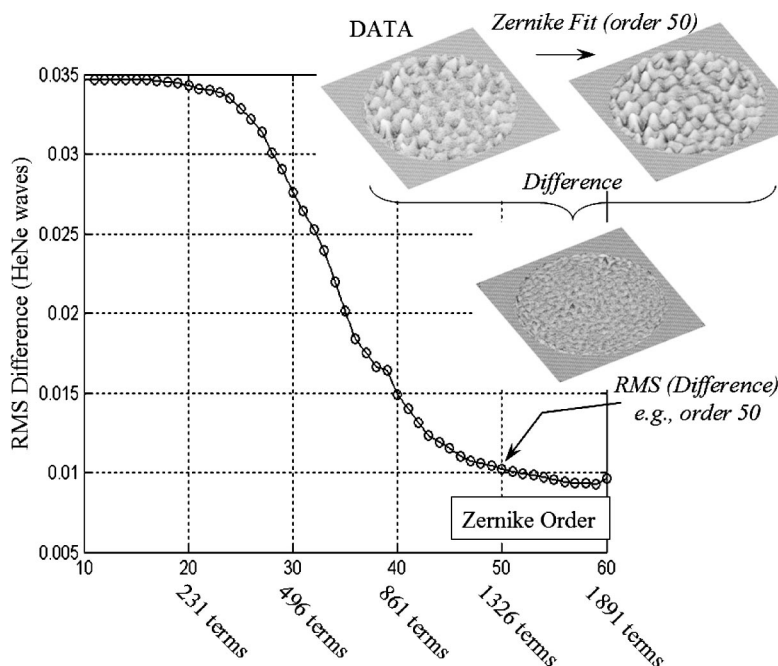

Fig. 17.   Rms (Zernike fit minus data) versus Zernike order for a deformable mirror "print-through" phase residual.
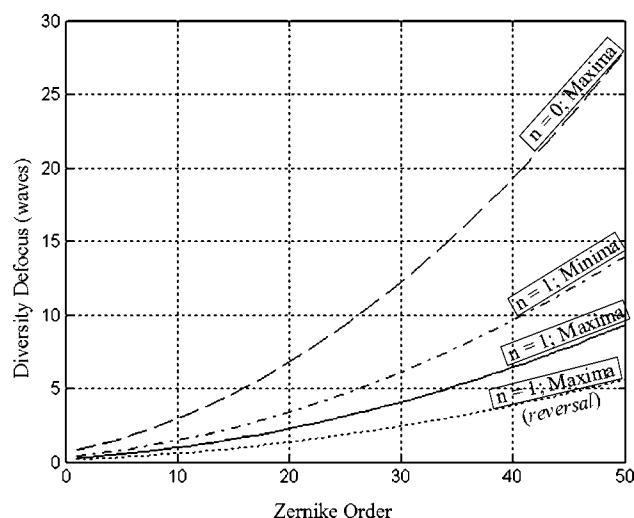
Fig. 18.   Diversity defocus values implied by Zernike basis order.

main advantage when the phase aberration consists of a single spatial-frequency component.   In (b), convergence is still the greatest performance increase, although somewhat slower than in (a) as a result of the more complicated spatial-frequency dependence of a low-order optical phase error compared with that of a pure sinusoid.   Finally, in (c), wavefront-sensing accuracy is more important than convergence when choosing between optimal and suboptimal diversity values.   The fact that larger-defocus values are generally better suited for higher-spatial-frequency recovery is simple to understand when one considers that larger-defocus intensity data (at least those avoiding minimum-contrast values) support higher spatial frequencies in the pupil.   Therefore it should not be too surprising that defocus settings tending to emphasize certain spatial frequencies will be optimal compared with those that do not.

An important conclusion is that no one diversity value is best for all wavefront-sensing applications.   Intelligent algorithm implementation is just as important as algorithm selection; i.e., by properly matching diversity values to the desired spatial frequency of recovery, one can potentially realize significant performance gains in both accuracy and convergence.   A corollary result is that proper diversity selection helps to emphasize a fundamental property for wavefront-sensing and -control systems, i.e., systems that are designed for lower-spatial-frequency recovery should be distinguished from those designed to recover higher-spatial-frequency aberrations.[13]

An additional characteristic is that since lower-spatial-frequency phase-retrieval systems require relatively small diversity defocus values, smaller PSF sizes can be exploited to minimize FFT array sizes when utilizing the iterative-transform approach.   Conversely, larger defocus values require additional array size.   As a result, the computational burden can generally be reduced for lower-spatial-frequency phase-retrieval systems.   Therefore building a "real-time" image-based wavefront sensor is more feasible based on the recovery of lower-spatial-frequency aberrations.

Finally, in an earlier analysis,[13] we have shown that the wavefront-sensing estimation burden increases as the

aberration spatial frequency increases.   This is simply a result of the fact that many more aberration coefficients must be estimated for higher-spatial-frequency recovery. In such cases, it is straightforward to show that if one utilizes a greater number of diversity images, the Cramér–Rao bound can be lowered,[5,13] leading to an improvement in wavefront-sensing performance when compared with that of the lower-spatial-frequency wavefront-sensing problem.   However, even in the lower-spatial-frequency case, the placement of two images on either side of focus is favorable for estimation, since an important cancellation occurs that can help to resolve confusion between a misplaced central obscuration and coma.[39]

REFERENCES AND NOTES

1. R. A. Gonsalves, "Phase retrieval and diversity in adaptive optics," Opt. Eng. **21**, 829–832 (1982).
2. The purpose of a diversity function in wavefront sensing is to "spread out" the optical response to expose aberration information.   Since defocus has only angular dependence, no one part of the point-spread function is emphasized more than any other.
3. J. R. Fienup, J. C. Marron, T. J. Schulz, and J. H. Seldin, "Hubble Space Telescope characterized by using phase-retrieval algorithms," Appl. Opt. **32**, 1747–1767 (1993).
4. J. R. Fienup, B. J. Thelen, R. G. Paxman, and D. A. Carrara, "Comparison of phase diversity and curvature wavefront sensing," in *Adaptive Optical System Technologies*, D. Bonaccini and R. Tyson, eds., Proc. SPIE **3353**, 930–940 (1998).
5. D. J. Lee, M. C. Roggemann, and B. M. Welsh, "Cramér–Rao analysis of phase-diverse wave-front sensing," J. Opt. Soc. Am. A **16**, 1005–1015 (1999).
6. H. L. Van Trees, *Detection, Estimation, and Modulation Theory* (Wiley, New York, 1968).
7. A. D. Whalen, *Detection of Signals in Noise* (Academic, New York, 1971).
8. S. M. Kay, *Fundamentals of Statistical Signal Processing* (Prentice-Hall, Englewood Cliffs, N.J., 1993).
9. R. V. Hogg and A. T. Craig, *Introduction to Mathematical Statistics*, 4th ed. (Macmillan, New York, 1978).
10. J. N. Cederquist, S. R. Robinson, D. Kryskowski, J. R. Fienup, and C. C. Wackerman, "Cramér–Rao lower bound on wavefront sensor error," Opt. Eng. **25**, 586–592 (1986).
11. J. N. Cederquist and C. C. Wackerman, "Phase-retrieval error: a lower bound," J. Opt. Soc. Am. A **4**, 1788–1792 (1987).
12. J. N. Cederquist, J. R. Fienup, C. C. Wackerman, S. R. Robinson, and D. Kryskowski, "Wave-front estimation from Fourier intensity measurements," J. Opt. Soc. Am. A **6**, 1020–1026 (1989).
13. B. H. Dean and R. Lyon, "Cramér–Rao bounds for focus diverse wavefront sensing with deformable mirror 'print-through'," in *Computational Optics and Imaging for Space Applications*, R. Lyon, ed. (NASA/Goddard Space Flight Center, Greenbelt, Md., 2000), pp. 127–142.
14. B. H. Dean, "Cramér–Rao analysis for phase-diverse-phase-retrieval: diversity functions and broadband phase-

retrieval," presented at the Wavefront Sensing & Controls Conference, sponsored by Kamuela Optical Associates, Kohala Coast, Hawaii, November 13–16, 2000.

15. J. R. Fienup, "Phase retrieval algorithms: a comparison," Appl. Opt. **21**, 2758–2769 (1982).

16. W. H. Southwell, "Wave-front analyzer using a maximum likelihood algorithm," J. Opt. Soc. Am. A **3**, 396–399 (1977).

17. W. B. Wetherell, "The calculation of image quality," in *Applied Optics and Optical Engineering*, R. Shannon and J. Wyant, eds. (Academic, New York, 1980), Vol. VIII, p. 172.

18. B. H. Dean, "Phase-retrieval performance as a function of defocus and aberration frequency," presented for the NASA Next Generation Space Telescope Technical Memoranda, NASA/Goddard Space Flight Center, Greenbelt, Md., August 20, 2000.

19. C. Bowers, "Some considerations regarding the propagation of spectral power from pupil to defocused image planes," presented for the NASA Next Generation Space Telescope Technical Memoranda, NASA/Goddard Space Flight Center, Greenbelt, Md., April 10, 2001.

20. B. H. Dean, "Fresnel zone propagation of spectral power with applications to image-based wavefront sensing," presented for the NASA Next Generation Space Telescope Technical Memoranda, NASA/Goddard Space Flight Center, Greenbelt, Md., July 8, 2001.

21. The frequency content in this instance is associated with the finite spacing of actuators placed in a periodic array behind a thin mirror face sheet. Ironically, the "print-through" associated with such systems is a result of the high-frequency correction capability of these many-actuator control systems. For example, for a Xinetics 349 channel deformable mirror, there are 21 actuators spanning the clear aperture, yielding approximately 10 cycles/aperture along a single spatial-frequency direction.

22. R. Paxman and B. Thelen, "Wavefront sensing for deployable-optic systems," presented at the Wavefront Sensing and Controls Conference, sponsored by Kamuela Optical Associates, Kohala Coast, Hawaii, November 13–16, 2000.

23. J. W. Goodman, *Introduction to Fourier Optics*, 2nd ed. (McGraw-Hill, New York, 1996), pp. 87–89.

24. W. Sun, "Cramér–Rao lower bound analysis on estimation accuracy for phase retrieval," M. S. thesis, directed by T. Schulz (Michigan Technological University, Houghton, Mich., 1998).

25. R. W. Gerchberg and W. O. Saxton, "A practical algorithm for the determination of phase from image and diffraction plane pictures," Optik (Stuttgart) **35**, 237–246 (1972).

26. D. L. Misell, "A method for the solution of the phase problem in electron microscopy," J. Phys. D **6**, L6–L9 (1973).

27. C. Roddier and F. Roddier, "Wavefront reconstruction from defocused images and the testing of ground-based optical telescopes," J. Opt. Soc. Am. A **10**, 2277–2287 (1993).

28. C. Roddier and F. Roddier, "Combined approach to the Hubble Space Telescope wavefront distortion analysis," Appl. Opt. **32**, 2992–3008 (1993).

29. J. R. Fienup, J. C. Marron, R. G. Paxman, T. J. Schulz, J. H. Seldin, and B. Thelen, "Image inversion analysis of the

Hubble Space Telescope," in *Final Report: Jet Propulsion Laboratory Contract 958892 on the Hubble Space Telescope Optical Telescope Assembly Analysis, August 1991* (Jet Propulsion Laboratory, Pasadena, Calif., 1991).

30. R. G. Lyon, "DCATT wavefront sensing and optical control study," Developmental Comparative Active Telescope Testbed Rep. WFSC-0001, February 22, 1999, http://jansky.gsfc.nasa.gov/OSCAR/.

31. D. Redding, S. Basinger, A. Lowman, F. Shi, P. Bely, R. Burg, and G. Mosier, "Wavefront sensing and control for a Next Generation Space Telescope," in *Space Telescopes and Instruments V*, P. Bely and J. Breckinridge, eds., Proc. SPIE **3356**, 758–772 (1998).

32. D. Redding, S. Basinger, A. Lowman, F. Shi, C. Bowers, L. Burns, P. Davila, B. Dean, M. Fitzmaurice, G. Mosier, B. Perkins, P. Petrone, T. Norton, M. Wilson, and L. Wheeler, "Wavefront control for a segmented deployable space telescope," in *UV, Optical, and IR Space Telescopes and Instruments*, J. B. Breckinridge and P. Jakobsen, eds., Proc. SPIE **4013**, 546–558 (2000).

33. B. H. Dean, "White-light phase-retrieval analysis," presented for the NASA Next Generation Space Telescope Technical Memoranda, NASA/Goddard Space Flight Center, Greenbelt, Md., October 11, 2000.

34. T. E. Gureyev, A. Roberts, and K. A. Nugent, "Phase retrieval with the transport-of-intensity equation: matrix solution with the use of Zernike polynomials," J. Opt. Soc. Am. A **12**, 1932–1941 (1995).

35. B. H. Dean and R. Boucarut, "Deformable mirror optical calibration and test results," presented at the Next Generation Space Telescope Science and Technology Exposition, Woods Hole, Mass., September 13–16, 1999.

36. C. Roddier and F. Roddier, "Reconstruction of Hubble Space Telescope wavefront distortion from stellar images taken at various focal positions," in *Final Report: Jet Propulsion Laboratory Contract 958893 on Hubble Space Telescope Optical Telescope Assembly Analysis, May 1991* (Jet Propulsion Laboratory, Pasadena, Calif., 1991), pp. 2–3.

37. D. Malacara and S. DeVore, "Interferogram evaluation and wavefront fitting," in *Optical Shop Testing*, D. Malacara, ed. (Wiley-Interscience, New York, 1997).

38. B. M. Levine, E. A. Martinsen, A. Wirth, A. Jankevics, M. Toledo-Quinones, F. Landers, and T. Bruno, "Horizontal line-of-sight turbulence over near-ground paths and implications for adaptive optics corrections in laser communications," Appl. Opt. **37**, 4553–4560 (1998).

39. If inaccurate pupil data are applied in the iterative-transform sense (Fig. 1), the pupil amplitude and the phase information become mixed, resulting in artificial aberrations in the phase estimate. For example, a pupil amplitude function consisting of a shifted central obscuration in a two-mirror system can lead to phase-retrieval estimates with artificial coma. But this ambiguity is resolved when utilizing diversity images on both sides of focus since the defocused PSF is asymmetric about focus (for a shifted central obscuration), while true coma produces a symmetric PSF about focus.